Zinc Oxide-Containing Porous Boron−Carbon−Nitrogen Sheets from Glycine−Nitrate Combustion: Synthesis, Self-Cleaning, and Sunlight-Driven Photocatalytic Activity

T. Bharathidasan,[‡] Aditya Mandalam,[‡] M. Balasubramanian, P. Dhandapani, S. Sathiyanarayanan, and Sundar Mayavan[*]

Centre for Innovation in Energy Research (CIER), CSIR−Central Electrochemical Research Institute, Karaikudi 630006, Tamil Nadu, India

S *Supporting Information*

ABSTRACT: We developed a single-step thermal method that enables successful inclusion of ZnO components in the porous boron−carbon−nitrogen (BCN) framework to form a new class of functional hybrid. ZnO-containing BCN hybrids were prepared by treating a mixture of B_2O_3, glycine, and zinc nitrate at 500 °C. Glycine−nitrate decomposition along with B_2O_3 acts as a source for ZnO-BCN formation. The incorporation of ZnO onto BCN has extended the photoresponse of ZnO in the visible region, which makes ZnO-BCN a preferable photocatalyst relative to ZnO upon sunlight exposure. It is interesting to note that as-prepared 2D ZnO-BCN sheets dispersed in PDMS form a stable coating over aluminum alloys. The surface exhibited a water contact angle (CA) of 157.6° with 66.6 wt % ZnO-BCN in polydimethylsiloxane (PDMS) and a water droplet (7 μL) roll-off angle of <6° and also demonstrates oil fouling resistant superhydrophobicity. In brief, the present study focuses on the gram scale synthesis of a new class of sunlight-driven photocatalyst and also its application toward the development of superhydrophobic and oleophobic coating.

KEYWORDS: *zinc oxide, combustion synthesis, superhydrophobic, self-cleaning, photocatalytic activity*
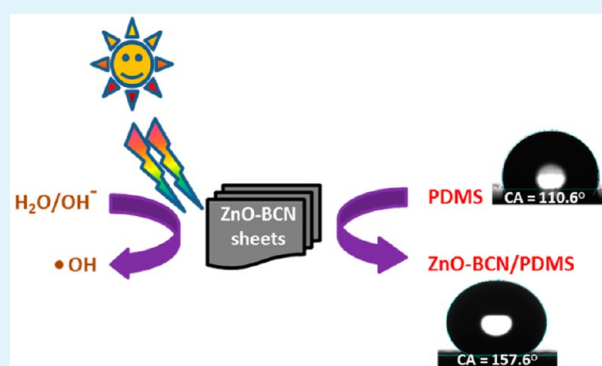
1. INTRODUCTION

Progress in materials science is strongly associated with the development of materials by energy-saving, environmentally friendly, and low-cost methods. Graphene and other two-dimensional materials such as boron nitride and boron carbon nitride have attracted more interest in the field of materials research because of many exceptional properties.[1−4] Similarly, metallic nanoparticles and oxides have attracted much attention due to their unique size-dependent properties.[5,6] The development of novel hybrid structures involving them is of significant interest. Such hybrid structures, which encompass the benefits of both host material and nanoparticles, can be of immense use for various potential applications. Although the synthesis and application of hybrid structures involving nanoparticles, graphene, and carbon nitride have been widely reported and well established,[7−9] there is much less discussion in the literature on the synthesis of hybrids involving boron carbon nitride (BCN) compounds. The applications of hybrid materials are essentially driven by progress in their production, and there are different methods to prepare hybrid nanomaterials. However, a search for new synthesis routes is still a field of immense research activity with focus on inexpensive, environmentally friendly, and scalable methods to produce novel nanohybrid materials.

Solution combustion synthesis (SCS) is an effective method for the synthesis of nanoscale hybrid materials and has been used in the synthesis of heterostructured nanocomposites for advanced applications.[10−12] Herein, we report for the first time an easy route for the synthesis of zinc oxide-containing porous boron−carbon−nitrogen hybrid sheets (ZnO-BCN) in a single-step process and the first investigation for self-cleaning and sunlight-driven photocatalytic properties. The synthesis is based on glycine−nitrate combustion, in combination with boron oxide at elevated temperature (see Materials and Methods). Our method enables the inclusion of metal oxide (zinc oxide (ZnO)) components in the BCN matrix toward formation of a new class of functional hybrids: metal oxide (ZnO)-containing boron carbon nitride compounds (ZnO-BCN). The as-prepared ZnO-BCN powder in water showed enhanced activity for bacteria degradation relative to pure ZnO upon direct sunlight exposure. It is interesting to note that as-prepared 2D ZnO-BCN sheets dispersed in PDMS form a stable coating over aluminum alloys. The coated films were investigated for their surface topography. The surface exhibited a water contact

angle (CA) of 157.6° and is achieved with 66.6 wt % ZnO-BCN in PDMS and an extremely low water adhesion with low contact angle hysteresis (6°). It is further interesting to note that superhydrophobic wetting behavior returns within minutes when a low surface tension liquid such as isooctane (γ = 18.77 mN/m) is added to surface. This synthesis has several advantages, such as availability of precursor materials, single-step process, no requirement of expensive or sophisticated instruments, gram scale yield, and, more importantly, scalability of the entire process.

2. MATERIALS AND METHODS

2.1. Materials. Boron oxide (B_2O_3), glycine (Gly), zinc nitrate ($ZnNO_3$), tetraethoxysilicate (TEOS), and polydimethylsiloxane (PDMS) silanol terminated (number-average molecular right (M_n = 110000), viscosity (~50000 cSt)) were procured from Sigma-Aldrich. Dibutyltin dilaureate was purchased from Alfa Aesar (Ward Hill, MA, USA).

2.2. Synthesis. Calculated quantities of B_2O_3, Gly, and $ZnNO_3$ were taken at a weight ratio of 1:2:2 (B_2O_3/Gly/$ZnNO_3$) and sonicated (in water) to form a homogeneous solution. The homogeneous solution was thermally treated at 500 °C for 2 h at 2 °C min^{-1} under an argon atmosphere to form ZnO-BCN sheets.

2.3. ZnO-BCN/PDMS Composite Films. The exfoliated ZnO-BCN was added to a mixture of 2.5 wt % PDMS (dissolved in toluene), TEOS (cross-linking agent for PDMS system), and dibutyltin dilaureate (catalyst for cross-linking) and magnetically stirred for 30 min. The resulting mixture was spray coated over aluminum and glass substrates at 20−25 psi with a film thickness of 10 μm.

2.4. Instrumentation. X-ray diffraction (XRD) data were measured on a Bruker D8 Advance X-ray diffractometer. FT-IR spectra were measured using a Nicolet 380 FTIR instrument with ATR. X-ray photoelectron spectroscopy (XPS) spectra were measured using a Sigma X-ray Photoelectron Spectrometer with an Al Kα X-ray source. Scanning electron microscope (SEM) images and energy-dispersive X-ray (EDX) spectra were taken on Carl Zeiss Supra 55VP/41/46 with an accelerating voltage of 15 kV using an SE detector. The UV−visible (UV−vis) absorption spectra and photoluminescence spectra (PL) were measured on a UV−vis-NIR spectrophotometer (Hitachi model U-4100) and a UV580C spectrophotometer, respectively. Surface area was studied using Autosorb iQ2 Quantachrome India. TEM images were recorded on Tecnai F20 (200 kV) field-emission transmission electron microscopy (FE-TEM). The production of OH radicals in ZnO-BCN suspensions under sunlight and dark conditions was analyzed by electron paramagnetic resonance (EPR) spectrometer (Bruker EMX Plus). The water contact angles (WCA) were measured by goniometer (OCA 35 Data Physics) in static mode employing Laplace−Young calculation. The observed WCA is the average of 10 measurements taken on different locations, and standard deviation was found to be ~±0.5°. The size of a water droplet in the wetting experiment is 7 μL. Both contact angle hysteresis (CAH) and roll-off angle were measured using standard methods reported earlier.[13]

2.5. Sunlight-Driven Antibacterial Activity. The strain of *Escherichia coli* used in this study was grown in nutrient broth (Himedia, Mumbai, India) overnight at 37 °C. Interaction between ZnO-BCN and bacterial cell surface and photokilling efficiency were investigated by solution suspension under direct sunlight illumination. A 10 mL suspension of ZnO-BCN (10 ppm) and bacterial culture (105 CFU/mL) in phosphate buffer solution (pH 7.0) was prepared and incubated in darkness for 15 min. After the 15 min incubation period, the media were exposed to dark and illuminated conditions for 30 min. Each sample was then subjected to total viable bacterial count by standard pour plate technique to calculate antibacterial activity (in percentage) using eq 1, where A is the viable count at 0 min and B is the viable count at 15, 30, 45, 60, or 75 min.

$$((A - B)/A) \times 100\% \tag{1}$$

Epi-fluorescence microscopy (E200 Coolpix -Nikon, Tokyo, Japan) was used to visualize the disruption of bacterial cell membrane as a function of incubation time. Dual stains of fluorescein isothiocyanate (FITC) and propidium iodide (PI) were used to identify living/dead bacterial cells. PI and FITC are selective to damaged cells and undamaged cell walls, which give rise to red and green emission, respectively. Bacterial samples were added to 0.5 μL of dual stain (1:1) and incubated for 15 min; excess stain was removed by rinsing with sterile distilled water.

Sunlight Source. Direct sunlight irradiation (of samples) was carried out in March 2015 in Karaikudi (CSIR-CECRI campus) in the afternoon between 1:00 and 3.0 p.m., and the temperature was around 29−31 °C.

3. RESULTS AND DISCUSSION

3.1. Characterization of ZnO-BCN. The XRD pattern of as-prepared ZnO-BCN (Figure 1) exhibits peaks at around 26° and 42°, which is similar to (002) and (100) lattice planes of BCNs reported previously with h-BN structures.[14]
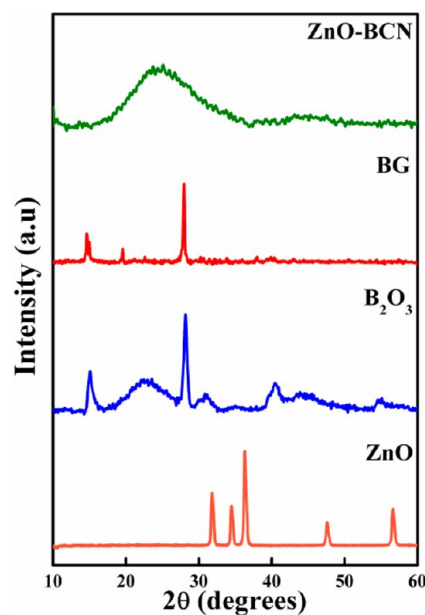
Figure 1. XRD patterns of ZnO ($ZnNO_3$ heated at 500 °C), B_2O_3, B_2O_3−glycine, and ZnO-BCN.

Interestingly, the XRD pattern of ZnO-BCN does not show any peak originating from zinc species, such as zinc oxide, zinc, zinc nitride, and zinc carbides. However, $ZnNO_3$ heated under similar conditions shows characteristic ZnO crystallite peaks. The nonobservance of Zn peaks for as-prepared samples indicates the presence of zinc species within BCN structures. Similar types of coordinated structures were reported by Wang et al.[15] and Liu et al.[16] in iron- and cobalt-containing carbon nitride compounds. In both cases peaks relating to iron and cobalt were not observed in XRD, but clear peaks were observed in XPS (as observed for our sample).[11] However, the exact nature of bonding/coordination is not known, and further characterization is essential to determine the local structure of zinc species. To better understand the role of $ZnNO_3$, the diffraction patterns of (BG) Gly-B_2O_3 (without $ZnNO_3$ and annealed at 500 °C) and B_2O_3 were analyzed. Almost all of the diffraction peaks of B_2O_3 are evident in BG, but after the addition of $ZnNO_3$ to BG (as in the case of prepared hybrid),

the B$_2$O$_3$ crystalline peaks disappeared completely and a broad diffraction peak at around 26° and 42° showed up. This indicates that ZnNO$_3$ addition is essential for B$_2$O$_3$ to react (or get consumed) via Gly−nitrate combustion.

Figure 2 shows the IR spectrum of as-prepared ZnO-BCN and B$_2$O$_3$. There is a broad peak around 1632 cm^{-1} indicating
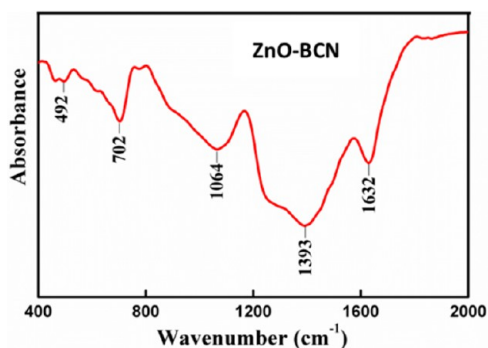

Figure 2. FTIR spectrum of ZnO-BCN.

C−N bond vibration. The peak at 1393 cm^{-1} corresponds to the B−N stretching mode of BCN.[10] The peak at 1064 cm^{-1} originates from the c-BN phase of boron carbon nitride.[12] The peaks at 492 and 702 cm^{-1} correspond to the stretching mode of Zn−O.[17] On the basis of the above FTIR result it may be said that ZnO-BCN hybrid structures are achieved. Raman spectra of ZnNO$_3$ heated at 500 °C (without glycine and B$_2$O$_3$) show first-order (fundamental) and second-order optical modes of ZnO (Figure 3a). Raman spectra of ZnO-BCN exhibit two broad amorphous peaks, corresponding to D (at 1355 cm^{-1}) and G (at 1581 cm^{-1}) bands of BCN structures along ZnO Raman modes. Raman spectra for ZnO and ZnO-BCN from 300 to 500 cm^{-1} are shown in Figure 3b. For ZnO, we observed wurtzite modes at 334, 386, 417, 439, and 584 cm^{-1} with an intense E2 (H) mode associated with the motion of oxygen atoms in ZnO at 439 cm^{-1}. High intense E2 (H) mode indicates its crystallinity.[18] The as-prepared ZnO-BCN also shows typical ZnO Raman modes, but the E2 (high) mode intensity of ZnO-BCN is significantly reduced (almost disappeared) relative to that of ZnO, indicating the lower or poor degree of crystallization.[18] The near disappearance or suppression of E2 (high) mode may be due to disorder induced by doping or substitution of B, N, or C in ZnO structure (or co-ordination of ZnO within the BCN matrix). The additional Raman modes at 640 and 743 cm^{-1} were observed in ZnO-

BCN, which can be attributed to the formation of ZnO phases involving B, C, or N (ZnO-BCN structures). Such additional Raman modes are a common feature for doped ZnO structures. Sudakar et al.[19] observed additional Raman modes for cobalt-doped ZnO between 600 and 800 cm^{-1}. Jothilakshmi et al.[20] observed additional Raman modes for lithium-doped ZnO associated with multiphonon processes at 651 and 737 cm^{-1}. Manjon et al.[21] reported anomalous bands in ZnO due to nitrogen local defects.

XPS characterizations were done to understand the bonding configurations in as-prepared hybrids. XPS survey scan (Figure 4a) of as-prepared ZnO-BCN revealed peaks due to boron, nitrogen, carbon, zinc, and considerable oxygen. The C 1s spectra (Figure 4b) of the as-prepared sample showed evidence of three chemical states, namely, C−C bond (major component), B−C bond, and C−O bond located at 284.8, 282.8, and 286.5 eV, respectively.[22,23] The N 1s spectra (Figure 4c) show a major single peak at 399.5 eV, which corresponds to the B−N bond.[23] The B 1s spectrum is shown in Figure 4 d. Many researchers[24,25] have reported that B−B bond at 188 eV as pure boron, the B−C bond at 190 eV as boron carbide, and the B−O bond at 190 eV as boron oxide. The B−O bond can be finely divided into BC$_2$O/BCO$_2$ and B$_2$O$_3$ bonds at 192.0 and 193.3 eV, respectively. The as-prepared sample C−O shows a major single peak at 192.3 eV, which indicates the presence of boron in the form of a B complex (BCO$_2$ or BC$_2$O bond).[26] The O 1s spectrum (Figure 4e) of the sample indicates the presence of three chemical states at 532.3 (major component), 530.8, and 528.4 eV, which correspond to the B−O bond, the Zn−O bond, O$_2^-$ in ZnO, respectively.[26] Figure 4f shows the Zn 2p spin−orbit split at 1022.45 eV (Zn 2p3/2) and 1045.7 eV (Zn 2p1/2) with an energy difference of 23.2 eV, which corresponds to Zn^{2+} in ZnO.[27] The presence of boron in the as-prepared sample was further confirmed by 11B solid state NMR spectroscopy. The peak at −3.48 ppm with equally spaced bands coincides with the results for doped boron (Figure S1).[28]

3.2. Morphology of ZnO-BCN. The SEM image (Figure 5a) reveals that the as-prepared structure is composed of a large number of fragmented nanosheets on a large sheet like structure with holes. EDS mapping was done to analyze the spatial distribution of elements in the as-prepared ZnO-BCN. The elemental mapping (Figure 5b−f) indicates homogeneous distribution of B, C, N, Zn, and O species, consistent with reported B−C−N structures.[29] The presence of B, C, N, O, and Zn species in ZnO-BCN was already confirmed by XPS (Figure
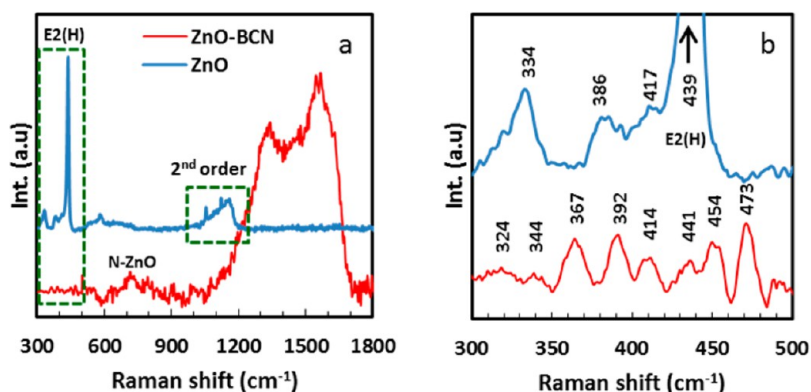

Figure 3. Raman spectra of (a) ZnO and ZnO-BCN and (b) ZnO and ZnO-BCN within the 300−500 cm^{-1} range.
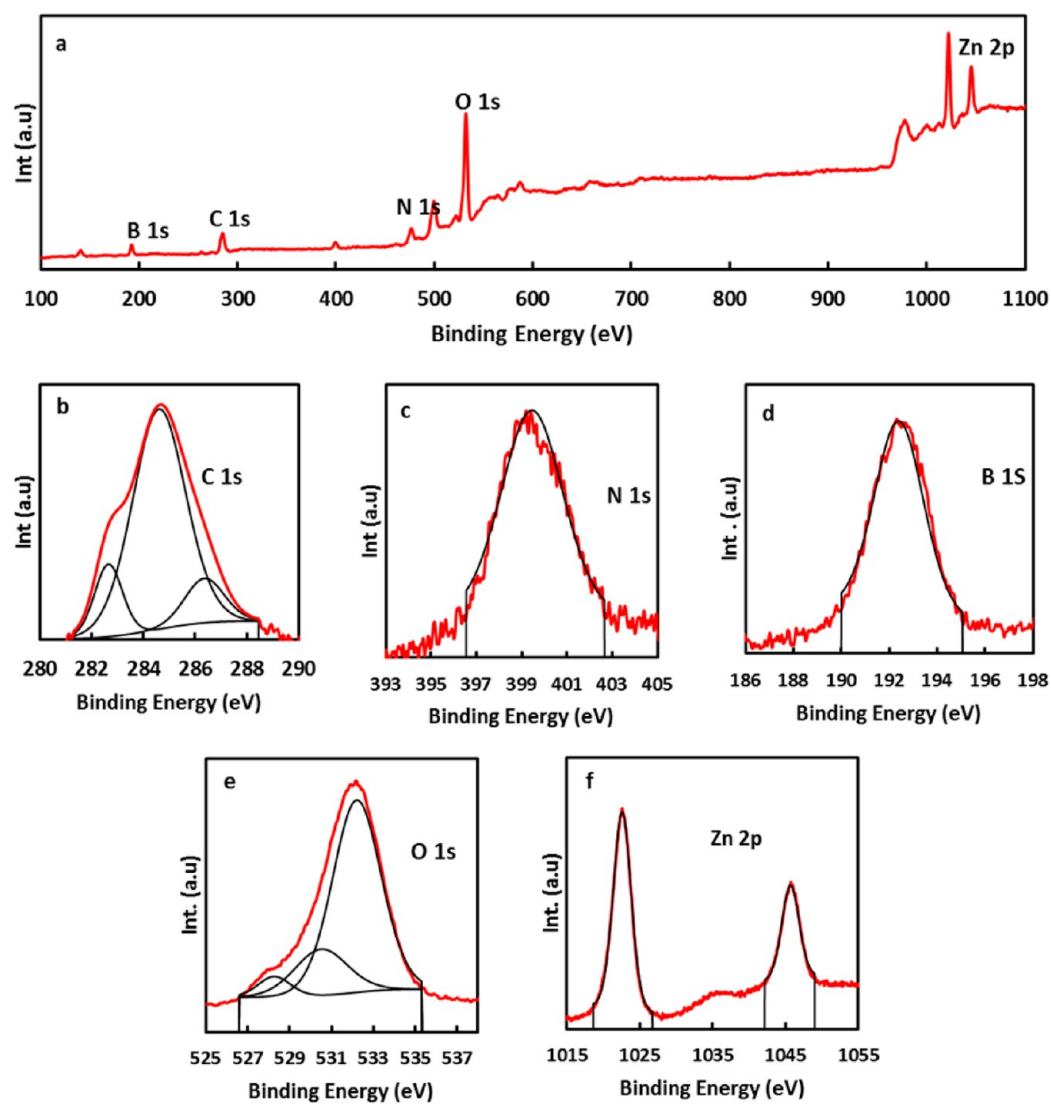
Figure 4. XPS spectra of ZnO-BCN: (a) survey scan; (b) C 1s; (c) B 1s; (d) N 1s; (e) O 1s; (f) Zn 2P.
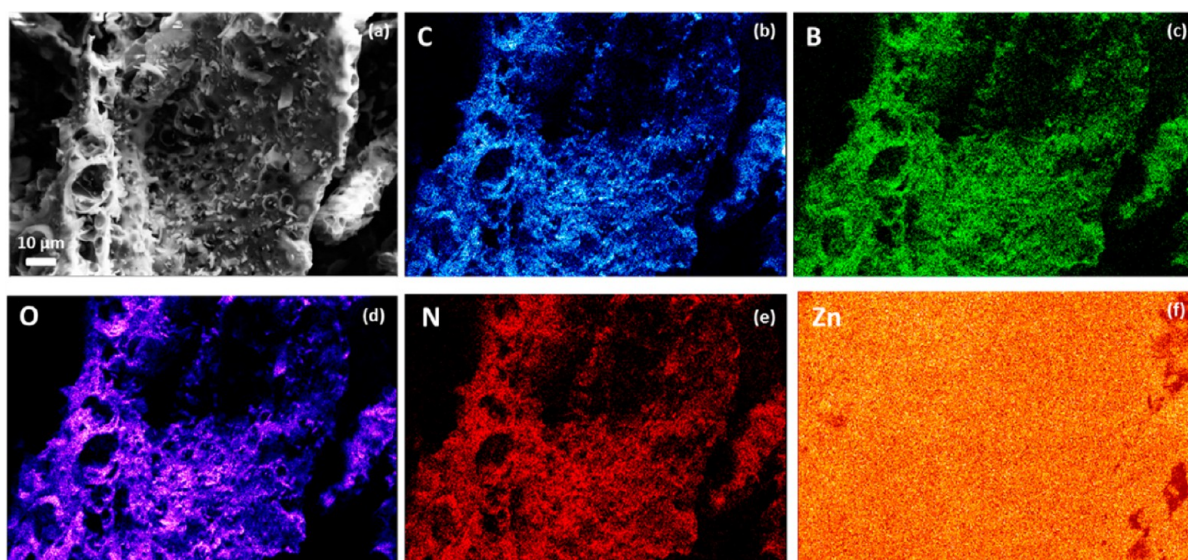

Figure 5. FE-SEM image of (a) ZnO-BCN hybrid and the corresponding EDX (b−f) maps of C, B, O, N, and Zn.

4a). Sonication was used as a top-down method to exfoliate stacked ZnO-BCN sheets. The exfoliation process involves cutting or direct peeling off from the as-prepared product. TEM was used to characterize the morphology of sonicated sample. TEM (Figure 6a,b) indicates the presence of porous BCN
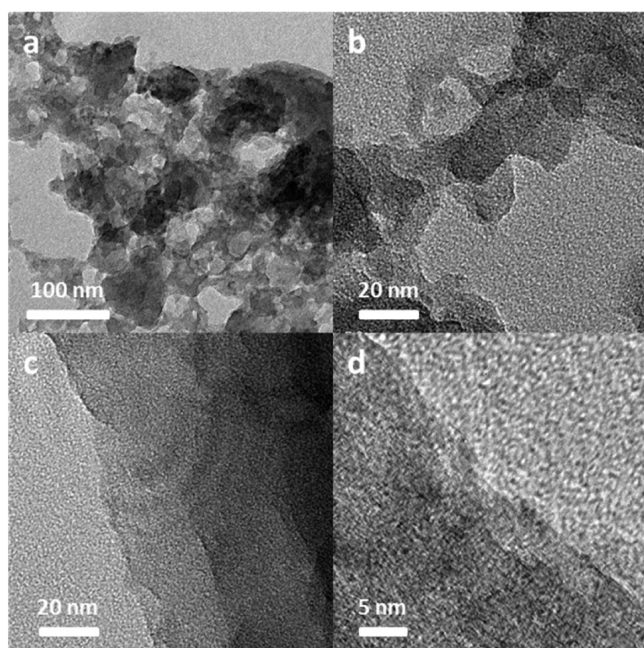
Figure 6. TEM images of ZnO-BCN sheets at different magnifications.

nanosheets (with pores ranging from 20 to 100 nm in diameter); the pores may be formed due to gas evolution upon thermal decomposition (formation mechanism in Scheme S1). Representative images (Figure 6c,d) show that the exfoliated ZnO-BCN sheet morphology resembles that of highly crumbled and randomly aggregated graphene-like sheets.[30] SAED pattern (Figure S2(a)) indicates the amorphous nature of the as-prepared ZnO-BCN hybrid. EDX spectra (Figure S2(b)) confirm the presence of B, C, N, O, and Zn species.

3.3. Optical Properties. The optical properties of the ZnO-BCN sheets annealed at 300 and 500 °C were evaluated by UV−visible absorption spectroscopy (Figure 7). Both samples were dispersed in water. It is seen that upon dispersion of ZnO-BCN prepared at 300 °C the solution turned yellow (inset of Figure 7). The yellow coloration indicates the
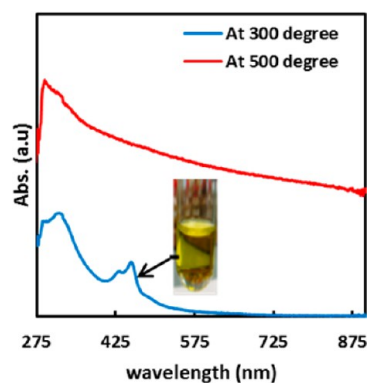
**Figure 7.** UV−visible absorption spectra of Gly−ZnNO$_3$−B$_2$O$_3$ annealed at 300 and 500 °C.

formation of ZnO as evidenced by distinctive absorption of ZnO with oxy-surface defects between 380 and 450 nm. However, the as-prepared sample (prepared at 500 °C) does not show any peak between 380 and 450 nm, and no yellow coloration is observed even after sonication for 2−3 h. This is an indication that in the as-prepared sample the zinc species (ZnO) are chemically coordinated to BCN (consistent with XRD data). It is interesting to note that the as-prepared ZnO-BCN hybrid (formed at 500 °C) exhibits excellent visible light absorption properties (Figure 7). This indicates that incorporation of ZnO onto the BCN extends the photoresponse of ZnO in the visible region due to strong interaction between BCN and ZnO.

3.4. Possible Formation Mechanism of ZnO-BCN. To ascertain the source of C and N, a control experiment was done by heating the mixture of Gly and B$_2$O$_3$ (without ZnNO$_3$) at 500 °C. The color of the resultant sample is dirty white (with B$_2$O$_3$-like crystalline XRD peaks), but the color was red-shifted (to black) when ZnNO$_3$ was included in the synthesis. XRD patterns typical of BCN structure (around 26°) are then obtained. Usually the presence of nanostructured carbons results in black composites and the colorful product obtained here provides an additional hint for atomic scale incorporation of carbon in the as-prepared compound.[31] These results clearly suggest that glycine and zinc nitrate combustion act as sources for C and N. The schematic illustration for the formation of ZnO-BCN sheets is shown in Scheme 1. The decomposition of Gly−nitrate occurred near 200 °C (Figure S3, TGA data). The decomposition results in the evolution of gases such as NO$_x$, NH$_3$, and CO$_x$, which may reduce B$_2$O$_3$ (as shown by XRD). The newly formed B species along with evolving gas may act as precursors for the bottom-up fabrication of porous/amorphous BCN sheets (as shown by TEM data). Simultaneously, ZnO species thermally diffuse into the BCN sheets to form ZnO-containing BCN sheets.

3.5. Sunlight-Driven Photocatalysis (Antibacterial Activity). With the confirmation of visible light absorbance, the as-prepared ZnO-BCN sample was tested for antibacterial activity at room temperature under direct sunlight. Figure 8a shows antibacterial activity in the presence of ZnO-BCN and ZnO at different intervals of time. Blank experiment (not shown here) was performed with bacteria in water under the same conditions without any catalyst (ZnO and ZnO-BCN) to exclude a possible photolysis of the bacteria under sunlight irradiation. No or very little bacterial degradation was observed in the absence of catalyst. The inhibition of bacterial growth with ZnO-BCN in sunlight is higher than with ZnO. In the case of ZnO-BCN, within 60 min of irradiation almost all bacteria were killed (Figure 8b,c). The production of OH radicals in ZnO-BCN suspensions under sunlight and dark conditions was analyzed by using an EPR method. It shows the presence of four distinct peaks, corresponding to hydroxyl radical generation, that are seen to be absent for ZnO-BCN under dark conditions (Figure S4). This observation offers a clear indication that the as-prepared ZnO-BCN is effective for the generation of hydroxyl radicals under direct sunlight illumination. The radicals generated are instrumental in facilitating the degradation of bacterial species. Many studies have indicated that the generation of reactive oxygen species (ROS) is the crucial factor influencing the activity of ZnO nanoparticles with respect to controlling bacterial growth. In the present study, light irradiation on ZnO-BCN leads to the generation of ROS at the particle surface, which attack *E. coli* bacterial cells in the

Scheme 1. Illustration of the Synthesis Procedure of ZnO-BCN Sheets
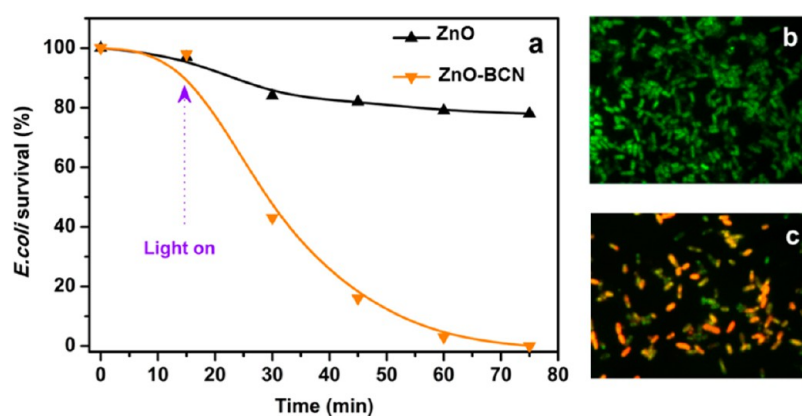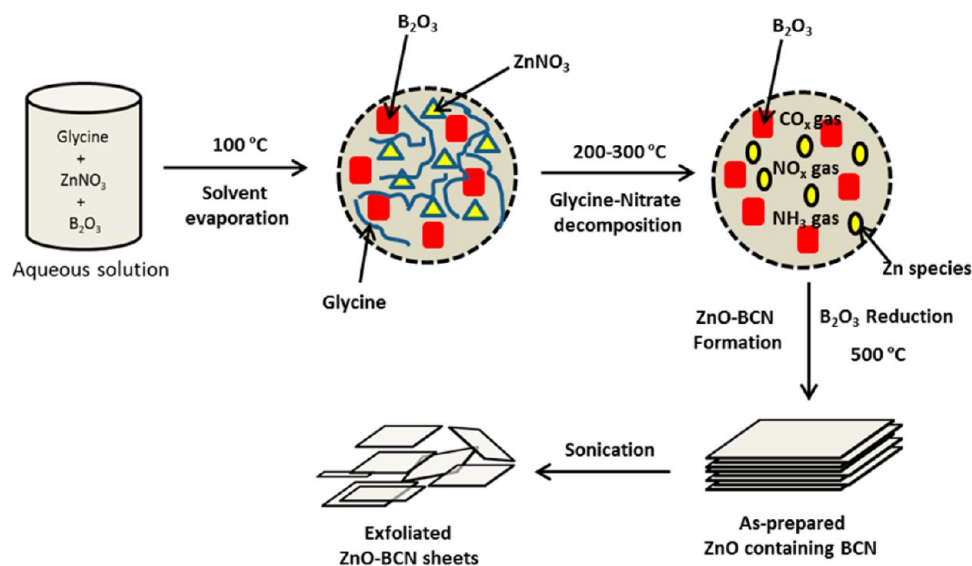
Figure 8. (a) Photoinactivation of *E. coli* under sunlight; epi-fluorescent microscopic images of *E. coli* (b) before light illumination and (c) after light illumination with ZnO-BCN.

vicinity and create micropits on the cell surface. This is expected to proceed through lipid peroxidation on bacterial cell membrane, resulting in cell membrane rupture, leakage of internal cellular contents, and cell death.[32−35] Because the extent of lipid peroxidation depends upon the production of ROS and its exposure to the bacterial cell membrane, greater radical generation upon sunlight results in enhanced antibacterial activity. Hence, in the present study, we conclude that ZnO-BCN-based material exhibits good antibacterial activity in the presence of sunlight by generation of ROS.

3.6. Photolumiscence Analysis. The photocatalytic efficiency of the catalyst is determined by electron–hole pair recombination kinetics, which can be experimentally determined by PL emission spectra. PL emission results from the recombination of free carriers, and hence PL with lower emission intensity indicates a lower recombination rate with higher separation efficiency. Figure 9 shows the PL spectra of ZnO and ZnO-BCN. A strong peak at ca. 400 nm was observed for ZnO alone due to local defect states.[36] For the as-prepared ZnO-BCN hybrid, the PL intensity (at ca. 400 nm) decreased greatly as compared to ZnO alone, indicating that the ZnO fluorescence could be quenched to a greater extent via bonding with BCN. Similar quenching behaviors have been observed in the past.[37] Therefore, attaching ZnO onto BCN (host)
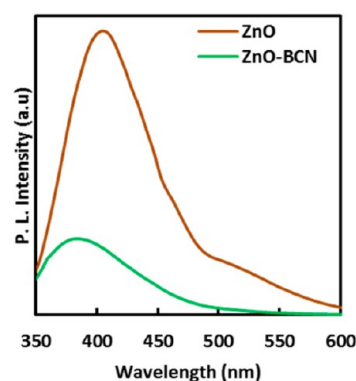
**Figure 9.** Photoluminescence (PL) spectra of ZnO and ZnO-BCN.

enhances the photocatalytic activity of ZnO in terms of inhibiting the recombination of photogenerated electron–hole pairs and accelerates the interfacial charge transfer process.[37] Hence, ZnO-BCN shows enhanced photocatalytic activity relative to ZnO alone. The surface area (SA) of ZnO and ZnO-BCN was measured using the BET isotherm. The SA of ZnO-BCN (24.17 m^2 g^{-1}) is almost three times that of ZnO (8.1 m^2 g^{-1}). The superior physicochemical properties of ZnO-
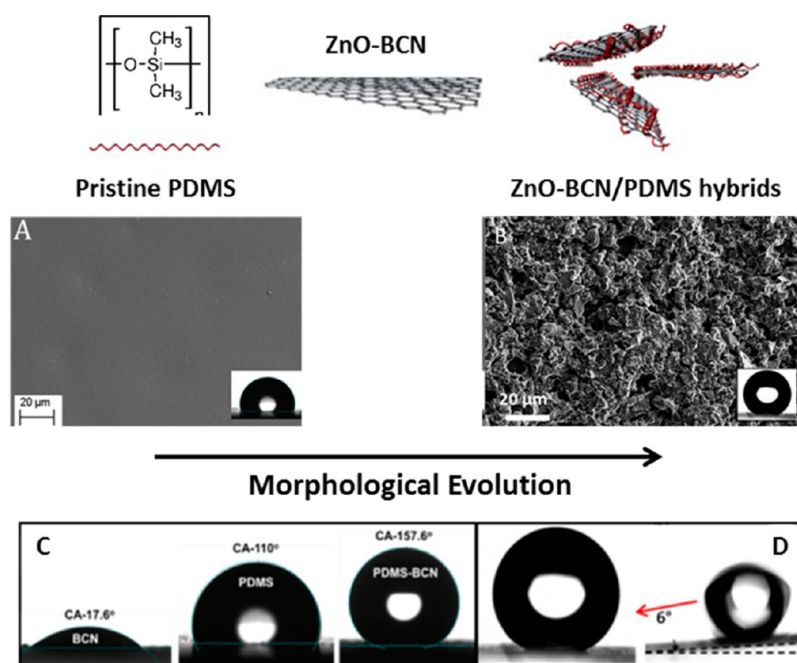
Figure 10. (A, B) Illustration of structural transition of hybrid films with respect to chemical composition of the as-prepared porous ZnO-BCN, as shown in SEM images. (C) Macroscopic images of water droplets (with contact angle) placed on ZnO-BCN, PDMS, and ZnO-BCN/PDMS coated surface. (D) Images of water droplet on ZnO-BCN/PDMS surface and a surface tilted by ∼6°, which induced drop rolling.

BCN nanosheets including larger SA and lower recombination kinetics (evidenced by PL data) contribute to its enhanced activity relative to ZnO for bacterial degradation.

3.7. Superhydrophobicity of ZnO–BCN/PDMS Polymeric Films. A general strategy for tuning the structure and surface morphology of PDMS toward achieving desired wettability is schematically represented in Figure 10a,b. Figure 10c shows the image of a water droplet placed on ZnO-BCN, PDMS, and ZnO-BCN/PDMS coated surfaces: WCAs as high as 157.6° were measured for the ZnO-BCN/PDMS hybrid (as compared to 17.6° and 110° for ZnO-BCN and PDMS, respectively). After incorporation of the optimum amount of ZnO-BCN in PDMS polymer matrix, the composite films exhibit the lesser wettability over the surface with CA of 157.6° and tilting angle of 6° (Figure 10d). Thus, by tuning the surface morphology of PDMS (by ZnO-BCN inclusion) the hydrophobicity of the films can be controlled. As shown in the SEM images of Figure 11, PDMS films with 66.6 wt % ZnO-BCN displayed a rough surface (Figure 11B−D). In contrast, the pristine PDMS film shows a smooth and flat surface (Figure 11A). The surface roughness of ZnO-BCN/PDMS hybrid films was analyzed by AFM. Hybrid films with 66.6 wt % ZnO-BCN revealed dual surface roughness pattern involving micro- and nanostructures with a thickness of 442 nm (Figure 11F). The effect of concentration (wt %) of ZnO-BCN on the wettability of the composite film is shown in Figure 12a. The Wenzel equation[38] ($\cos \theta r = r \cos \theta s$) has been used extensively to understand the WCA dynamics at a rough solid interface. (In the equation, r, θr, and θs correspond to roughness factor and WCA values on a rough surface and a smooth surface, respectively). Water drops on blank PDMS and PDMS with 33% BCN are in the Wenzel state. In this regime, water drops are assumed to pin on the air pockets and solid−liquid interaction is particularly strong in their contact line. With an increase in ZnO-BCN concentration to 50%, the surface exhibited a WCA of 152.5° and a sliding angle of 11°.
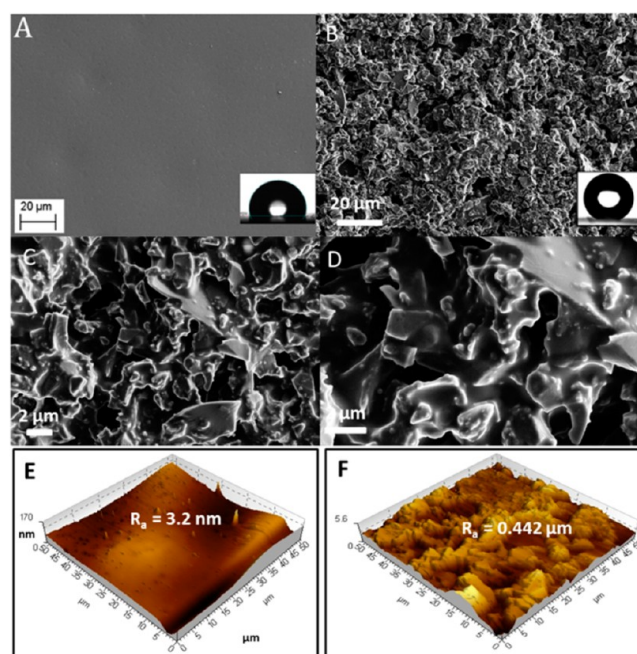
Figure 11. Field-emission scanning electron microscopy (FE-SEM) images of (A) pristine PDMS, (B−D) ZnO-BCN/PDMS coated on Al substrate; AFM images of (E) PDMS and (F) ZnO-BCN/PDMS coated on an Al substrate.

Furthermore, at 66.6 wt % ZnO-BCN concentration the surface exhibited a WCA of 157.6° and a sliding angle of about 6°, indicating perfect nonwetting behavior. The roughness created on the surface with increased ZnO-BCN might be sufficient to trap air inside the voids of the surface. This causes a heterogeneous surface composed of both air and solid, which reduces the adhesive force between the water and solid surface; for this case the contact angle is described in terms of the
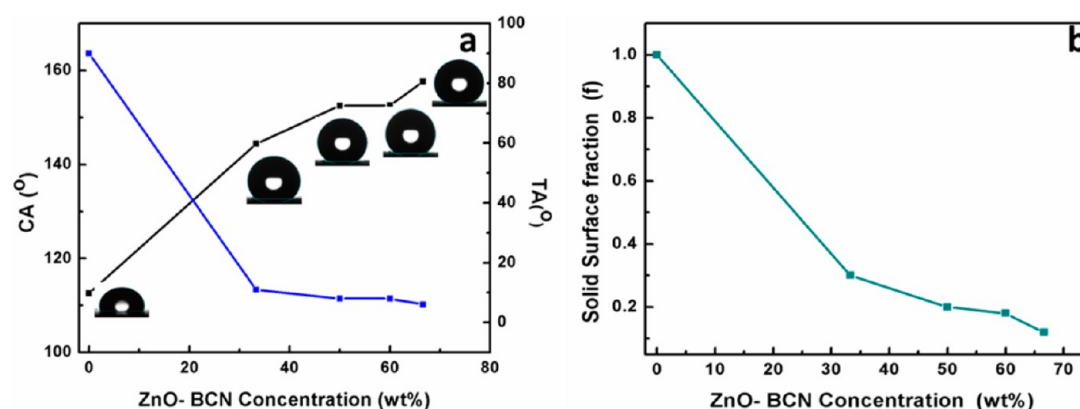
Figure 12. (a) Variation of contact and tilting angle (blue line) with different concentrations of ZnO-BCN (wt %); (b) solid fraction value (f) on films.

Cassie−Baxter equation.[39] $\cos \theta r = f1 \ (\cos \theta s + 1) - 1$ describes the behavior of a water drop on a heterogeneous rough surface, where $f1$ is the surface area fraction of the solid, and θr and θs are the CA on rough and smooth surfaces, respectively. Hence, at high ZnO-BCN concentration the Cassie state dominates over the Wenzel state. The increase in ZnO-BCN concentration created a rough surface and a dual roughness pattern (as evidenced by AFM and SEM data; Figure 11), which is sufficient enough to trap a lot of air, resulting in a large water−air interface-like surface that offers high resistance against wetting, leading to superhydrophobicity.[40,41]

In addition, the superhydrophobicity was also explained by solid fraction and work of adhesion relation. The solid surface fraction (f) value derived from Cassie's equation is found to be 1.00, 0.3, 0.2, 0.18 and 0.12 for 0, 33.3, 50, 60, and 66.6 wt % respectively, as shown in Figure 12b. A low solid fraction value (with increase in ZnO-BCN concentration) ensures that water droplets are being exposed to a large portion of air that wards off water from wetting the surface and water maneuvers with a low sliding angle. Young-Dupre's equation[42] ($\cos \theta = (\gamma SA - \gamma SL)/\gamma LA = (W/\gamma LA) - 1$) was used to calculate the work of adhesion (adhesion strength between water droplet and surface). The work of adhesion and WCA are vice versa. In Figure S5 the work of adhesion and contact angles for water ($\gamma - 72.9$ mN/m) is plotted versus BCN concentration. The work of adhesion is found to be 44.90, 13.6, 8.23, 8.16, and 5.45 mN/m for 0, 33.3, 50, 60, and 66.6 wt % respectively, resulting in extremely low WSA.

In general, hydrophobic surfaces (which tend to repel water) have a strong affinity toward nonpolar or oily liquids that can even negate the superhydrophobic behavior of the surface. Hence, developing surfaces with both superhydrophobic and superoleophobic properties is essential. The antifouling performance was analyzed by placing drops of low surface tension liquids (such as cyclohexane, methyl ethyl ketone, and isooctane) on the ZnO-BCN/PDMS-coated samples; they wet the surface instantly, but superhydrophobicity was restored within 60 s (Figure 13). Antifouling performance is due to the PDMS matrix, which is capable of absorbing a range of organic liquids as discussed in the literature.[43,44]

In general, highly expensive and toxic fluoro polymers were used to generate superamphiphobic behavior, but our approach is distinct as we could achieve superamphiphobic behavior with an inexpensive non-fluoro approach. By using our approach it is possible to prepare metal-decorated hybrids by selecting a
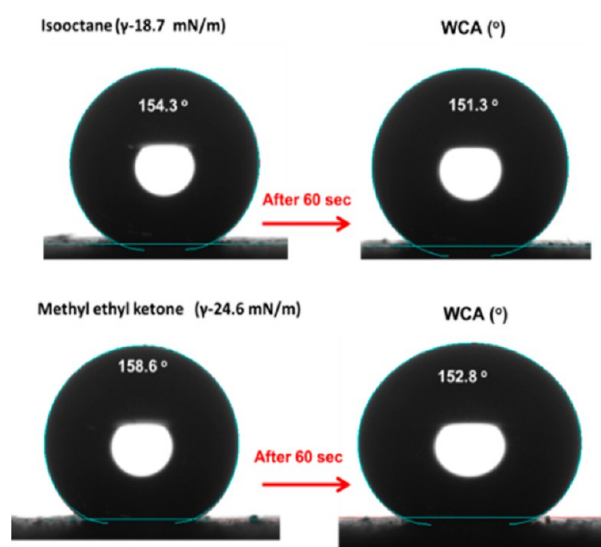
Figure 13. Anti-oil-fouling performance of ZnO-BCN/PDMS-coated surface.

suitable metal nitrate. As a proof of concept, silver nitrate was used as a metal source to synthesize silver nanoparticle (ca. 10−15 nm) decorated BCN nanosheets (Ag-BCN) (Figure 14). Through our work, we have demonstrated that Gly−nitrate combustion can be used as a precursor toward the synthesis of nanoparticles or semiconductors containing porous BCN sheets.
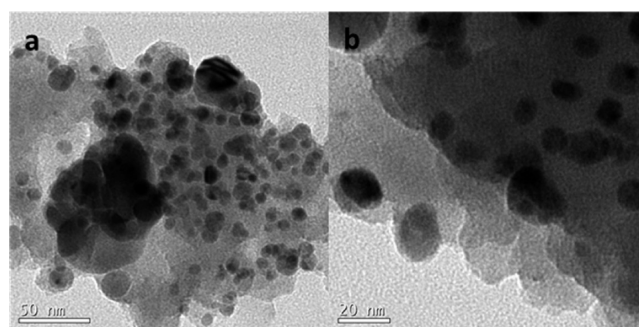
Figure 14. TEM images of Ag nanoparticle decorated BCN sheets.

4. CONCLUSIONS

We have demonstrated (with mechanism) that metal oxide, here represented by ZnO, can be incorporated into the BCN matrix by a one-step process involving glycine−nitrate combustion. The as-prepared material absorbs visible light and is capable of degrading bacteria under direct sunlight irradiation. BCN sheets have been used for the first time to prepare a stable coating over aluminum substrates. The substrates (with 66.6 wt % ZnO-BCN) showed a WCA of 157.6° and a WSA of 6° and are oleophobic. Through our approach it is possible to create a range of metal or metal oxide containing BCN hybrids for a variety of applications.

■ ASSOCIATED CONTENT

Ⓢ Supporting Information

The Supporting Information is available free of charge on the ACS Publications website at DOI: 10.1021/acsami.5b04609.

NMR, EDX, and EPR spectra and work of adhesion plot of ZnO-BCN/PDMS (PDF)

■ AUTHOR INFORMATION

Corresponding Author

*(S.M.) Phone: 91-4565-241453. E-mail: sundarmayavan@cecri.res.in.

Author Contributions

‡T.B. and A.M. contributed equally.

Author Contributions

The manuscript was written through contributions of all authors. All authors have given approval to the final version of the manuscript.

Notes

The authors declare no competing financial interest.

■ ACKNOWLEDGMENTS

■ REFERENCES

(1) Zheng, Y.; Liu, J.; Liang, J.; Jaroniec, M.; Qiao, S. Z. Graphitic Carbon Nitride Materials: Controllable Synthesis and Applications in Fuel Cells and Photocatalysis. *Energy Environ. Sci.* 2012, 5, 6717−6731.

(2) Thomas, A.; Fischer, A.; Goettmann, F.; Antonietti, M.; Muller, J. O.; Schlogl, R.; Carlsson, J. M. Graphitic Carbon Nitride Materials: Variation of Structure and Morphology and Their Use as Metal-Free Catalysts. *J. Mater. Chem.* 2008, 18, 4893−4908.

(3) Rao, C. N. R.; Gopalakrishnan, K.; Maitra, U. Comparative Study of Potential Applications of Graphene, MoS_2, and Other Two-Dimensional Materials in Energy Devices, Sensors, and Related Areas. *ACS Appl. Mater. Interfaces* 2015, 7, 7809−7832.

(4) Chung, C.; Kim, Y.-K.; Shin, D.; Ryoo, S.-R.; Hong, B.-H.; Min, D.-H. Biomedical Applications of Graphene and Graphene Oxide. *Acc. Chem. Res.* 2013, 46, 2211−2224.

(5) Daniel, M. C.; Astruc, D. Gold nanoparticles: Assembly, SupramolecularChemistry, Quantum-Size-Related Properties, and Applications Toward Biology, Catalysis, and Nanotechnology. *Chem. Rev.* 2004, 104, 293−346.

(6) Katz, E.; Willner, I. Integrated Nanoparticle−Biomolecule Hybrid Systems: Synthesis, Properties, and Applications. *Angew. Chem., Int. Ed.* 2004, 43, 6042−6108.

(7) Zhang, N.; Zhang, Y.; Xu, Y.-J. Recent Progress on Graphene-based Photocatalysts: Current Status and Future Perspectives. *Nanoscale* 2012, 4, 5792−5813.

(8) Cheng, N.; Tian, J.; Liu, Q.; Ge, C.; Qusti, A. H.; Asiri, A. M.; Al-Youbi, A. O.; Sun, X. Au-Nanoparticle-Loaded Graphitic Carbon Nitride Nanosheets: Green Photocatalytic Synthesis and Application toward the Degradation of Organic Pollutants. *ACS Appl. Mater. Interfaces* 2013, 5, 6815−6819.

(9) Jin, J.; Fu, X.; Liu, Q.; Zhang, J. A Highly Active and Stable Electrocatalyst for the Oxygen Reduction Reaction based on a Graphene-Supported $g-C_3N_4$@Cobalt Oxide Core−Shell Hybrid in Alkaline Solution. *J. Mater. Chem. A* 2013, 1, 10538−10545.

(10) Li, F. T.; Wang, Q.; Ran, J.; Hao, Y. J.; Wang, X.; Zhao, D.; Qiao, S. Ionic Liquid Self-Combustion Synthesis of $BiOBr/Bi_{24}O_{31}Br_{10}$ Heterojunctions with Exceptional Visible-Light Photocatalytic Performances. *Nanoscale* 2015, 7, 1116−1126.

(11) Li, F. T.; Wang, Q.; Wang, X.; Li, B.; Hao, Y.; Liu, R.; Zhao, D. In-situ One-step Synthesis of Novel $BiOCl/Bi_{24}O_{31}Cl_{10}$ Heterojunctions via Self-Combustion of Ionic liquid with Enhanced Visible-Light Photocatalytic Activities. *Appl. Catal., B* 2014, 150−151, 574−584.

(12) Li, F. T.; Zhao, Y.; Hao, Y. J.; Wang, X. J.; Liu, R. H.; Zhao, D. S.; Chen, D. M. N-Doped P25 TiO_2-Amorphous Al_2O_3 Composites: One-Step Solution Combustion Preparation and Enhanced Visible-light Photocatalytic Activity. *J. Hazard. Mater.* 2012, 239-240, 118−127.

(13) Bharathidasan, T.; Narayanan, T. N.; Sathyanaryanan, S.; Sreejakumari, S. S. Above 170° Water Contact Angle and Oleophobicity of Fluorinated Graphene Oxide Based Transparent Polymeric Films. *Carbon* 2015, 84, 207−213.

(14) Lei, W.; Qin, S.; Liu, D.; Portehault, D.; Liu, Z.; Chen, Y. Large Scale Boron Carbon Nitride Nanosheets with Enhanced Lithium Storage Capabilities. *Chem. Commun.* 2013, 49, 352−354.

(15) Wang, X.; Chen, X.; Thomas, A.; Fu, X.; Antonietti, M. Metal-Containing Carbon Nitride Compounds: A New Functional Organic−Metal Hybrid Material. *Adv. Mater.* 2009, 21, 1609−1612.

(16) Liu, Q.; Zhang, J. Graphene Supported $Co-g-C_3N_4$ as a Novel Metal−Macrocyclic Electrocatalyst for the Oxygen Reduction Reaction in Fuel Cells. *Langmuir* 2013, 29, 3821−3828.

(17) Khatoon, S.; Ganguly, A.; Ahmad, T. Fabrication of Nano-Sized Solid Solution of $Zn1−xMn_xO$ (x = 0.05, 0.10, 0.15) in Reverse Microemulsions: Structural Characterization and Properties. *Bull. Mater. Sci.* 2012, 35, 377−382.

(18) Lin, C. C.; Young, S. L.; Kung, C. Y.; Horng, L.; Chen, H. Z.; Kao, M. C.; Shih, Y. T.; Ou, C. R. Phonon Spectra and Magnetic Behaviors of Hydrothermally Synthesized Sm-Doped ZnO Nanorods. *Vacuum* 2013, 87, 178−181.

(19) Sudakar, C.; Kharel, P.; Lawes, G.; Suryanarayanan, R.; Naik, R.; Naik, V. M. Raman Spectroscopic Studies of Oxygen Defects in Co-Doped ZnO Films Exhibiting Room Temperature Ferromagnetism. *J. Phys.: Condens. Matter* 2007, 19, 026212.

(20) Jothilakshmi, R.; Ramakrishnan, V.; Thangavel, R.; Kumar, J.; Sarua, A.; Kuball, M. Micro-Raman Scattering Spectroscopy Study of Li-Doped and Undoped ZnO Needle Crystals. *J. Raman Spectrosc.* 2009, 40, 556−561.

(21) Manjon, F. J.; Mari, B.; Serrano, J.; Romero, A. H. Silent Raman Modes in Zinc Oxide and Related Nitrides. *J. Appl. Phys.* 2005, 97, 053516.

(22) Wang, S.; Zhang, L.; Xia, Z.; Roy, A.; Chang, D. W.; Baek, J. B.; Dai, L. BCN Graphene as Efficient Metal-Free Electrocatalyst for the Oxygen Reduction Reaction. *Angew. Chem., Int. Ed.* 2012, 51, 4209−4212.

(23) Zhang, X.; Lu, Z.; Lin, J.; Fan, Y.; Li, L.; Xu, X.; Hu, L.; Meng, F.; Zhao, J.; Tang, C. Spectra Properties of BCNO Phosphor Prepared by a Two-Step Method at Low Sintering Temperature. *ECS J. Solid State Sci. Technol.* 2013, 2, R39−R43.

(24) Yoshikawa, A.; Kikuchi, Y.; Suda, T.; Ashikawa, N.; Nishimura, K.; Sagara, A.; Noda, N.; Oya, Y.; Okuno, K. Chemical Behavior of

Hydrogen Isotopes into Boronized Film in LHD. *J. Nucl. Mater.* **2009**, *386−388*, 367−370.

(25) Kikuchi, Y.; Yang, Y.; Yoshikawa, A.; Suda, T.; Sagara, A.; Noda, N.; Oya, Y.; Okuno, K. Study on Retention Behavior and Chemical States of Energetic Deuterium Implanted into Carbon-Contained Boron Film. *J. Nucl. Mater.* **2009**, *386−388*, 371−374.

(26) Shao, D.; Li, J.; Tan, X.; Yang, Z.; Okuno, K.; Oya, Y. XPS Investigation of Impurities Containing Boron Films Affected by Energetic Deuterium Implantation and Thermal Desorption. *J. Nucl. Mater.* **2015**, *457*, 118−123.

(27) Prakash, A.; Misra, S. K.; Bahadur, D. The Role of Reduced Graphene Oxide Capping on Defect Induced Ferromagnetism of ZnO Nanorods. *Nanotechnology* **2013**, *24*, 095705−095712.

(28) Vineesh, T. V.; Praveen Kumar, M.; Takahashi, C.; Kalita, G.; Alwarappan, S.; Pattanayak, D. K.; Narayanan, T. N. Bifunctional Electrocatalytic Activity of Boron-Doped Graphene Derived from Boron Carbide. *Adv. Energy Mater.* **2015**, DOI: 10.1002/aenm.201500658.

(29) Zhou, J.; Li, N.; Gao, F.; Zhao, Y.; Hou, L.; Xu, Z. Vertically-Aligned BCN Nanotube Arrays with Superior Performance in Electrochemical Capacitors. *Sci. Rep.* **2014**, *4*, 6083.

(30) Li, X.; Hao, X.; Zhao, M.; Wu, Y.; Yang, J.; Tian, Y.; Qian, G. Exfoliation of Hexagonal Boron Nitride by Molten Hydroxides. *Adv. Mater.* **2013**, *25*, 2200−2205.

(31) Lei, W.; Portehault, D.; Dimova, R.; Antonietti, M. Boron Carbon Nitride Nanostructures from Salt Melts: Tunable Water-Soluble Phosphors. *J. Am. Chem. Soc.* **2011**, *133*, 7121−7127.

(32) Li, Y.; Zhang, W.; Niu, J.; Chen, Y. Mechanism of Photogenerated Reactive Oxygen Species and Correlation with the Antibacterial Properties of Engineered Metal-Oxide Nanoparticles. *ACS Nano* **2012**, *6*, 5164−5173.

(33) Li, Y.; Niu, J.; Zhang, W.; Zhang, L.; Shang, E. Influence of Aqueous Media on the ROS-Mediated Toxicity of ZnO Nanoparticles toward Green Fluorescent Protein-Expressing *Escherichia coli* under UV-365 Irradiation. *Langmuir* **2014**, *30*, 2852−2862.

(34) Tong, G.-X.; Du, F.-F.; Liang, Y.; Hu, Q.; Wu, R.-N.; Guan, J.-G.; Hu, H. Polymorphous ZnO Complex Architectures: Selective Synthesis, Mechanism, Surface Area and Zn-Polar Plane-Codetermining Antibacterial Activity. *J. Mater. Chem. B* **2013**, *1*, 454−463.

(35) Kumar, R.; Anandan, S.; Hembram, K.; Rao, T. N. Efficient ZnO-Based Visible-Light-Driven Photocatalyst for Antibacterial Applications. *ACS Appl. Mater. Interfaces* **2014**, *6*, 13138−13148.

(36) Kong, Y. C.; Yu, D. P.; Zhang, B.; Fang, W.; Feng, S. Q. Ultraviolet-Emitting ZnO Nanowires Synthesized by a Physical Vapor Deposition Approach. *Appl. Phys. Lett.* **2001**, *78*, 407−409.

(37) Ajay Rakkesh, R.; Durgalakshmi, D.; Balakumar, S. Efficient Sunlight-Driven Photocatalytic Activity of Chemically Bonded GNS−TiO$_2$ and GNS−ZnO Heterostructures. *J. Mater. Chem. C* **2014**, *2*, 6827−6834.

(38) Wenzel, R. N. Resistance of Solid Surfaces to Wetting by Water. *Ind. Eng. Chem.* **1936**, *28*, 988−994.

(39) Cassie, A B D.; Baxter, S. Wettability of Porous Surfaces. *Trans. Faraday Soc.* **1944**, *40*, 546−551.

(40) Choi, B. G.; Park, H. S. Superhydrophobic Graphene/Nafion Nanohybrid Films with Hierarchical Roughness. *J. Phys. Chem. C* **2012**, *116*, 3207−3211.

(41) Miwa, M.; Nakajima, A.; Fujishima, A.; Hashimoto, K.; Watanabe, T. Effects of the Surface Roughness on Sliding Angles of Water Droplets on Superhydrophobic Surfaces. *Langmuir* **2000**, *16*, 5754−5760.

(42) Nosonovsky, M.; Bhushan, B. Multiscale Friction Mechanisms and Hierarchical Surfaces in Nano- and Bio-tribology. *Mater. Sci. Eng., R* **2007**, *58*, 162−193.

(43) Zhang, J.; Pu, G.; Severtson, S. J. Fabrication of Zinc Oxide/Polydimethylsiloxane Composite Surfaces Demonstrating Oil-Fouling-Resistant Superhydrophobicity. *ACS Appl. Mater. Interfaces* **2010**, *2*, 2880−2883.

(44) Lee, J. N.; Park, C.; Whitesides, G. M. Solvent Compatibility of Poly(dimethylsiloxane)-Based Microfluidic Devices. *Anal. Chem.* **2003**, *75*, 6544−6554.